

Article

Physical Model Test on the Deformation and Fracturing Process of Underground Research Laboratory during Excavation and Overloading Test

Chuancheng Liu ^{1,2,*}, Xikui Sun ¹, Xiufeng Zhang ¹, Qiangyong Zhang ², Yang Chen ¹ and Jinxi Wang ³

¹ Shandong Energy Group Co., Ltd., Jinan 250014, China; sunxikui@shandong-energy.com (X.S.); zhangxiufeng@shandong-energy.com (X.Z.); chenyang@shandong-energy.com (Y.C.)

² School of Civil Engineering, Shandong University, Jinan 250100, China; qiangyongzdsu@163.com

³ China Energy Engineering Group, Guangdong Electric Power Design Institute Co., Ltd., Guangzhou 510663, China; wangjinxi@gedi.com.cn

* Correspondence: liuchuancheng@shandong-energy.com

Abstract: Understanding the excavation-induced deformation and failure behaviors of the URL (underground research laboratory) for the geological disposal of HLW (high-level radioactive waste) before its construction is essential due to its high safety requirements. To reveal the interaction between structures, the effect of supporting and the characteristics of the overloading-induced damage and safety factor, we carried out a physical model test on the deep underground chamber groups consisting of one main roadway and two parking lots (one is supported, the other is not supported), and the engineering background is the URL of HLW for the geological disposal in Beishan. This type of geomechanical model test is still the first to be carried out so far. The test results confirm that the chamber group is generally stable during the excavation process. After the excavation, the displacement of the intersection is 7–33% larger than that of the non-intersection. The displacement of the supported chamber is reduced by 14–22% compared with that without support. The tension of the bolt at the vault top is greater than that at the waist of the cave. Without support, the safety coefficient of crack initiation is 1.7; the safety coefficient of local destruction is 2.1; and the safety coefficient of general demolition is 2.3. In contrast, the safety coefficient of crack initiation is 1.9; the safety coefficient of local destruction is 2.2; and the safety coefficient of general demolition is 2.4 when the rock mass is supported. The research results provide an important basis for optimizing design schemes and evaluating the safety of the construction process for URL.

Keywords: physical model test; overall safety factor; bolt support; large section chamber; failure modes; geological disposal; radioactive waste



check for updates

Citation: Liu, C.; Sun, X.; Zhang, X.; Zhang, Q.; Chen, Y.; Wang, J. Physical Model Test on the Deformation and Fracturing Process of Underground Research Laboratory during Excavation and Overloading Test. *Sustainability* **2023**, *15*, 9416. <https://doi.org/10.3390/su15129416>

Academic Editors: Yaxun Xiao, Yanchun Yin and Haitao Li

Received: 11 April 2023

Revised: 4 June 2023

Accepted: 6 June 2023

Published: 12 June 2023



Copyright: © 2023 by the authors. Licensee MDPI, Basel, Switzerland. This article is an open access article distributed under the terms and conditions of the Creative Commons Attribution (CC BY) license (<https://creativecommons.org/licenses/by/4.0/>).

1. Introduction

A power shortage has become a principal question in many coastal areas accompanied by the rapid development of China's economy. Faced with this situation, the Chinese government has changed its policy on the development of nuclear power and many new nuclear power plants have been constructed or are under construction [1]. However, fast development of nuclear power causes an emergency challenge, i.e., the total amount of high-level radioactive waste that needs to be disposed of will reach 83,000 tons by 2050 [2]. The safe disposal of the HLW is an important task for sustainable development and environmental protection. The safest and most feasible method is deep geological disposal [2,3].

The underground engineering of burying HLW is called deep geological repositories (DGRs) whose service life should be at least 1×10^4 a because waste in a repository is toxic and has a long half-life. This requirement is not considered in the projects encountered previously. The development of DGRs is a long-term and systematic process, which

generally involves basic research, site evaluation of repositories, URL study, repository design, construction and closure [4].

The URL is an essential key facility linking the various procedures during the development of DGRs [3]. The purposes of URL construction are to ultimately evaluate the long-term performance and safety of DGR through various studies [2]. So far, a number of URLs have been constructed around the world [5–8]. To satisfy the many functions, most URLs are deeply buried and have relatively complex layouts. For instance, the Meuse/Haute-Marne URL in France consists of two levels of experimental drifts at depths of 445 m and 490 m, which consist of two shafts and drift networks [9]; the Äspö Hard Rock Laboratory in Sweden consists of a shaft, a spiral ramp and horizontal roadways with a maximum burial depth of 420 m [10].

Therefore, it is necessary to master the construction technology of DGRs, to understand the effects of various factors on the disposal system and to evaluate the performance of the repository barrier. A large number of laboratory experiments and in situ tests have been carried out, for instance, research on the site characteristic evaluation method including the new technology, method and equipment for obtaining rock and groundwater characteristics of sites [11–13]; study on the manufacturing and performance of the engineering barrier such as to obtain the chemical and physical properties of the artificial barrier and cushioning materials [14–17]; the service life prediction and corrosion behavior disposal cans [18–20]; study on the excavation technology of DGRs such as the excavation technology [21,22] and equipment performance [23] of DGRs with minimum damage to surrounding rock; study on the effect of radioactive waste disposal such as the disposal cans and the cushioning materials' responses under coupled thermo-hydro-mechanical conditions [24,25]; and the radionuclide migration test including diffusion and adsorption of radionuclides in rocks and their migration with the rock fissure flow [26–28], etc.

Numerical simulation has become quite mature and achieved very good results [29]. However, the structure of URL is generally complex and deep-buried; it is difficult to simulate the rupture process of surrounding rock by numerical modeling, and the simulation of overall structural safety is not perfect. Conducting in situ tests is limited by their high costs. In contrast, the physical model test plays an important part in the study of geotechnical engineering [30].

So far, physical model experiments have been extensively applied on excavation processes and the support of underground chambers with remarkable achievements obtained [31–33]. For instance, in the aspect of experimental means, Shin et al. [34] carried out model tests on the Umbrella Arch Method while Hu et al. [35] carried out tests on the Pipe-Roofing Method, which verified the rationality of these construction methods; in the aspect of experimental equipment, Bao et al. [36] proposed a multi-scale method to simulate the test model of shield tunnels, Zhu et al. [37] researched and developed a 3D physical model test system and Li et al. [38] realized 3D loading of physical model experiments; in the aspect of measurement methods, Lin et al. [39] and Wang et al. [40] applied the acoustic emission (AE) monitoring system to model experiments, while Chen et al. [41] applied photogrammetry and laser scanning to measure tunnel deformation. Zhang et al. [42] and Zhu et al. [43] used displacement sensing rods based on fiber Bragg gratings and multi-point extensometers to measure the displacement of surrounding rock in model experiments; in the aspect of the support system, Zhu et al. [43] achieved construction simulation of the pre-stressed cable and rock bolt in physical model experiments and Nunes and Meguid [44] studied the effect of the hard layer covering the tunnel on the stress generated in the tunnel lining through model experiments. All of these studies have greatly promoted the development of physical model experiments.

Many previous model tests were subject to the following limitations: most of them were planar or quasi-three-dimensional, which cannot simulate the real state of in situ stress; the size of most of the experimental systems was small, which can only simulate a single chamber rather than complex chamber groups; and most mining was performed manually, resulting in low accuracy and having a negative impact on test results. To

overcome these limitations, we have carried out 3D geomechanical model tests [31] and overloading tests [45]. Different from our previous tests, the objective of this study was to assess the interaction between chambers, integral stability and the supporting anchorage effect of the π -shaped intersection chamber composed of one circular main roadway and two three-core arch parking lots. In addition, the characteristics of the overloading-induced damage and safety factor of the whole system were estimated through the overloading test.

2. Project Overview

The pre-selected location for China's first URL for deep geological disposal of HLW is located in the Beishan area of Gansu Province, Northwestern China.

The terrain of this area is mainly composed of flat Gobi and small hills with the elevation ranging from 1400 m to 2000 m. In situ tests confirmed that the in situ stress can be calculated from the depth (H) as follows:

$$\left. \begin{aligned} \sigma_H &= 0.0305H \text{ (MPa)} \\ \sigma_h &= 0.0208H \text{ (MPa)} \\ \sigma_v &= 0.0268H \text{ (MPa)} \end{aligned} \right\} \quad (1)$$

where σ_H is the maximum horizontal principal stress; σ_h is the minimum horizontal principal stress; and σ_v is the vertical stress [31,45,46].

Figure 1a shows the preliminary design scheme of the Beishan URL, which consists of one ramp, three shafts and two-level experiment chambers [2]. The experiment chambers will be located on two levels, namely the main level of -560 m and the auxiliary level of -240 m. In order to study the stability, supporting effect and overloading safety of the typical large section of chambers, we select two parking lots at the depth of 560 m and the main roadway intersecting with them as the research target (Figure 1b). The scale of the prototype is $125 \text{ m} \times 125 \text{ m} \times 100 \text{ m}$. In this range, there are one main roadway (diameter of 7 m) and two parking lots (cross-section size of $12 \text{ m} \times 9 \text{ m}$) (see Figure 1c).

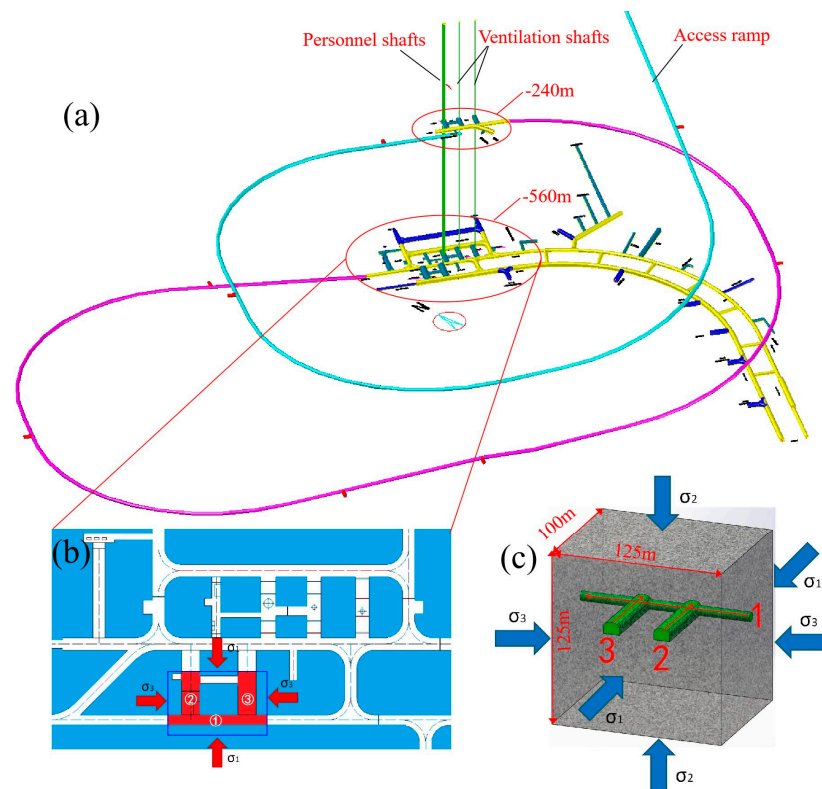


Figure 1. (a) The preliminary design scheme of the URL in Beishan, China (from Ref. [1]). (b) Simulation range of the prototype (source: modified from Ref. [45]). (c) The prototype structure.

3. Physical Model Test

3.1. Similarity Principles

According to the similitude theory, the following relationships should also be satisfied [31,45,47]:

$$C_{\sigma} = C_{\gamma} C_L \quad (2)$$

$$C_{\delta} = C_{\varepsilon} C_L \quad (3)$$

$$C_{\sigma} = C_{\varepsilon} C_E \quad (4)$$

$$C_{\varepsilon} = C_f = C_{\varphi} = C_{\mu} = 1 \quad (5)$$

where C_E , C_{ε} , C_{δ} , C_L , C_{γ} , C_{σ} , C_f , C_{φ} and C_{μ} are the similarity coefficients of the elastic modulus, strain, displacement, geometry, volume–weight, stress, coefficient of friction, frictional angle and Poisson’s ratio, respectively.

Based on the scale of the test system and the range of the project, the similarity coefficient of geometry C_L was selected to be 50. The overall dimension of the analogue model is 2500 mm × 2500 mm × 2000 mm, accordingly. The analogue model consists of the main roadway (with a diameter of 140 mm) and two parking lots (with the cross-section size of 240 mm × 180 mm) (see Figure 2). The physical model test was conducted using the 3D physical model test system. Photos of the system can be found in Figure 3 and more details about it can be found in our previous publications [31,45].

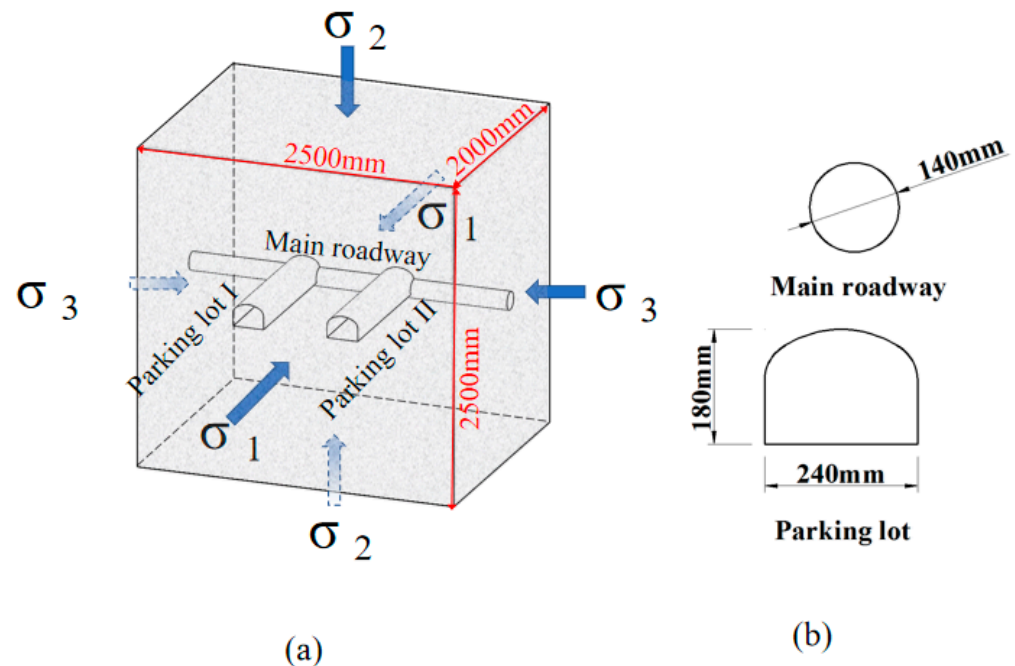


Figure 2. (a) Layout of the chamber group considered in the physical model test. (b) Cross-section of the main roadway and the parking lot.

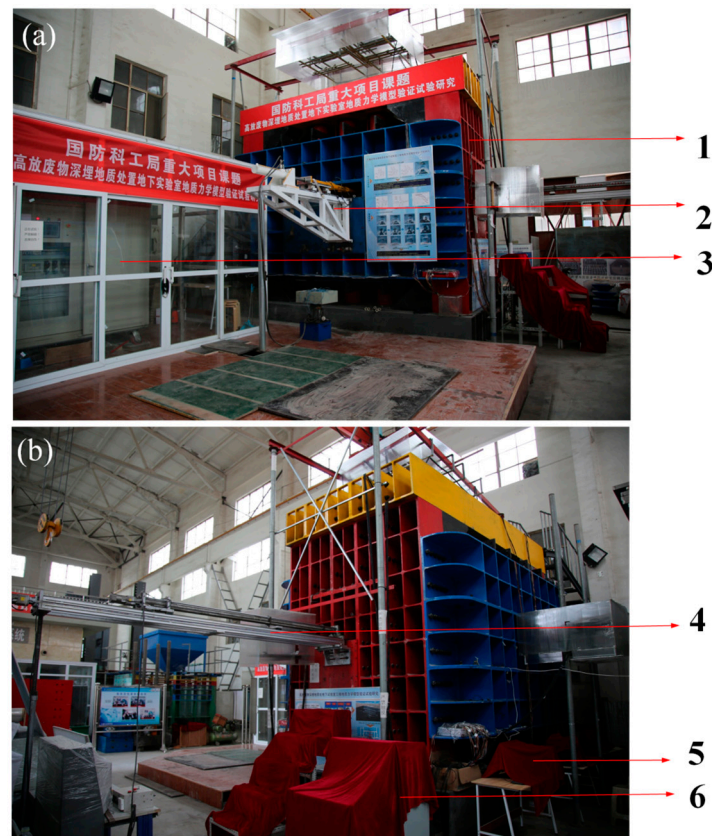


Figure 3. Photos of the model test system. (a) Frontal view of the system. (b) Side view of the system. 1—The reversed force device of loading; 2—Miniature TBM automatic excavation device for the three-core arch cave; 3—Intelligent hydraulic loading control system; 4—Miniature TBM automatic excavation device for the circular cave; 5—The automatic stress–strain monitoring system; 6—The automatic displacement monitoring system.

3.2. Development of the Similar Materials

3.2.1. Similar Materials of Surrounding Rock

One of the most important prerequisites to conduct a geomechanical model test is that the similar materials should behave similarly with the real rock. We used the IBSCM (iron–barites–silica cementation material) [31,45] as the similar material of surrounding rock in this study.

The similarity coefficient of volume–weight C_γ was selected to be 1. Then, the similarity coefficients of other parameters could be determined according to Equation (3). Table 1 shows the mechanical and physical parameters of the original rock and the similar materials, respectively. Table 2 shows the mix proportion of the similar materials.

Table 1. Mechanical and physical parameters.

Parameters	Uniaxial Compressive Strength (u_{cs}) (MPa)	Tensile Strength (τ) (MPa)	Deformation Modulus (E_0) (GPa)	Cohesion (c) (MPa)	Friction Angle (φ) ($^\circ$)	Poisson's Ratio (μ)	Unit Weight (γ) (kN/m 3)
Original rock	132.37	6.86	49.17	28.13	50.6	0.264	26.80
Similar materials (calculated from similarity principles)	2.647	0.134	0.983	0.563	50.6	0.264	26.80
Similar materials (measured by experiments)	2.611~2.683	0.123~0.142	0.955~0.992	0.541~0.571	49.9~50.6	0.25~0.27	26.2~27.1

Table 2. The mix proportion of the similar materials (from refs. [31,45]).

Similar Scale	I:B:S	Concentration (%)	Proportion of Mass of Binder (%)
$C_L = 50$	1:0.45:0.25	18	6

I, B and S refer to the proportion of the refined iron powder, the barite powder and the quartz sand, respectively.

3.2.2. Simulation of the Support

Three types of materials were normally used in previous studies to simulate bolts in model tests: metal materials (aluminum wire, iron wire, copper wire, tin wire, etc.), plant reinforcements (bamboo, wood, etc.) and composite materials (glass fiber, nylon rod, high-pressure polyethylene, etc.) [30]. The grouting materials were simulated by a cement slurry, gypsum slurry and high-concentration alcohol rosin silicone oil solvent [31,45]. In this study, semi-hardened aluminum wire (2 mm in diameter) was used to simulate the bolt with the consideration of the similarity of the bolt length, elasticity modulus, yield strength and tensile strength. The high-concentration rosin alcohol solution was selected as the grouting material. The properties of the prototype and analogue bolt are listed in Table 3.

Table 3. Parameters of the original bolt and the analogue bolt.

Parameters	Length (L) (m)	Elastic Modulus (E) (GPa)	Yield Strength (σ_s) (MPa)	Tensile Strength (σ_t) (MPa)
Original bolt	2.5	206	315	490
Analogue bolt	0.05	3.7	6.3	8.21

3.3. Construction of the Physics Model

3.3.1. Construction Procedures

The physical model was paved, compacted and air-dried layer-by-layer to ensure the integrity and homogeneity of the surrounding rock [48–53].

Due to the limitation of the bolt installation technology and model chamber size, the bolt support is frequently simulated by pre-embedding the bolt [31,50,52]. The detailed procedures of pre-embedding the bolt are as follows: determining the position of pre-embedding the bolt (see Figure 4a); drilling holes in the position of the pre-embedded bolt (see Figure 4b); inserting similar materials of the bolt (see Figure 4c); injecting grouting similar materials (see Figure 4d); and air-drying grouting similar materials. Three sections of bolts are selected as monitoring objects and strain gauges are pasted in the middle of the bolts.

3.3.2. Installation of the Monitoring Sensors

Figure 5 shows the positions of the monitoring sensors in the test. All monitoring sensors are installed at the key parts in five monitoring sections. The main steps to install the sensors can be found in Figure 6.

3.4. Model Excavation

Once the physical model was constructed, 3D gradient loading was applied on its boundaries to simulate the in situ stress at a depth of 560 m. A realistic initial stress state calculated from Equation (1) was applied, as shown in Figure 1c. Constant initial stresses were applied on the model for 24 h, so as to form a stable initial stress field within the model.

The in situ stress of the whole model remained constant during the entire excavation process. The sequence of excavation is as follows: the main roadway, upper step of parking lot II, lower step of parking lot II, upper step of parking lot I and lower step of parking lot I. Table 4 shows the excavation controlling parameters in the model test. The mini automatic excavation device is used for chamber group excavation.

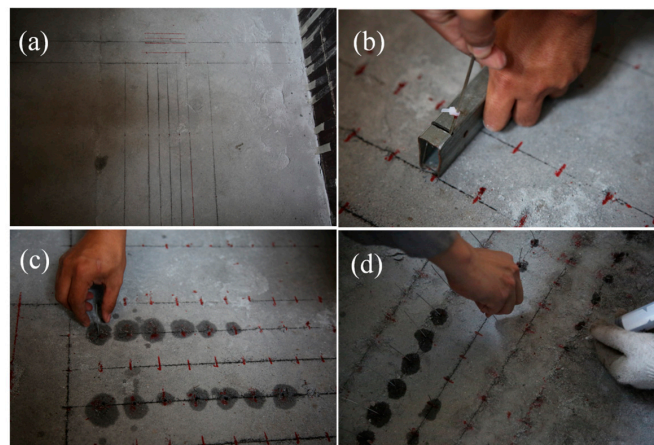


Figure 4. The general procedure of pre-embedding the bolt. (a) Determine the position of pre-embedding the bolt. (b) Drill holes in the position of the pre-embedded bolt. (c) Insert similar materials of the bolt. (d) Grouting similar materials are injected.

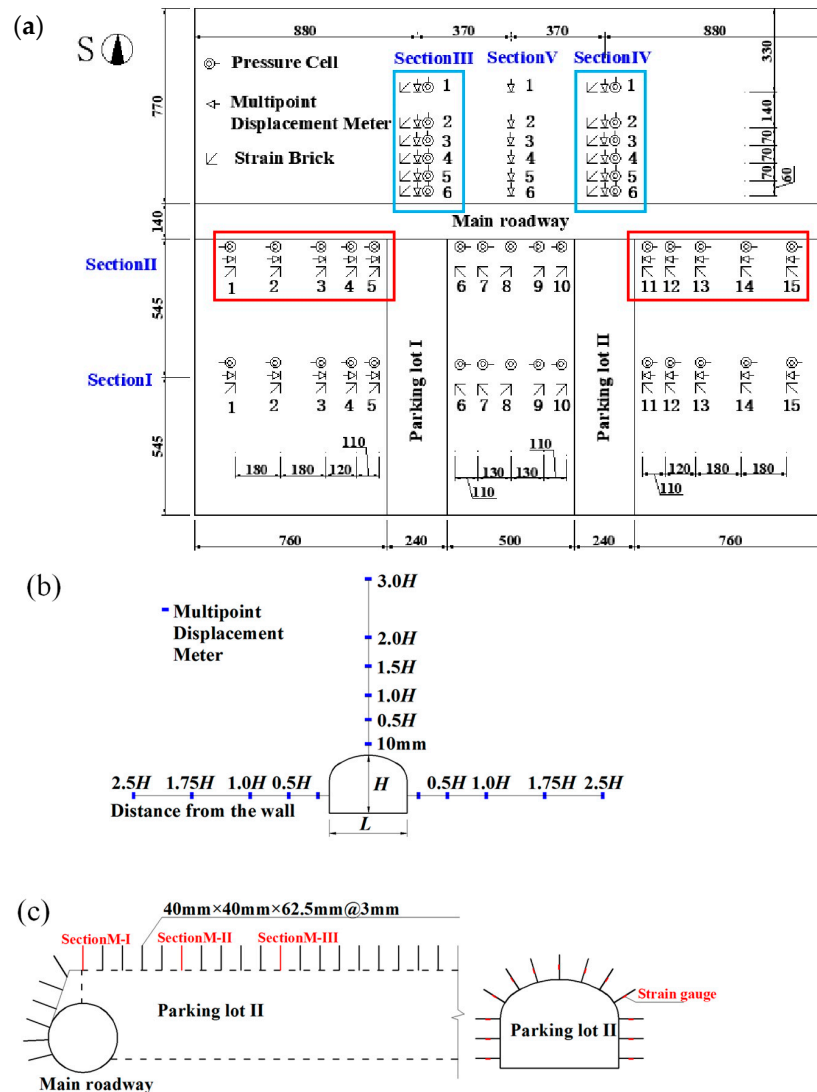


Figure 5. (a) Plan layout design drawing of sensors. (b) Section layout design drawing of sensors. (c) Schematic layout of monitoring sensors for bolts.



Figure 6. The main steps to install the sensors. (a) Position by total station. (b) Determine the outline of the caves. (c) Install the displacement sensors. (d) Install the grating ruler connected to the displacement sensors. (e) Install the strain brick. (f) Install the pressure cell.

Table 4. The excavation controlling parameters in the model test.

Order of Excavation	Length (mm)	Excavation Method	The Advance Rate (mm/step)	Number of Steps
1. Main roadway	2500	Full section	40	60
2. Parking lot II	1090	Upper and lower steps	40	56
3. Parking lot I	1090	Upper and lower steps	40	56

3.5. Test Results

In this section, in order for the convenience of the analysis and research, we converted all the test data obtained from the physical model experiments into prototypes.

3.5.1. Test Results of Surrounding Rock

Figures 7 and 8 show the variations of the radial displacements in the different sections of the chamber group, respectively.

From these results, we can conclude the following:

Variation of radial displacement is basically consistent with the phenomena from previous tests [40,41]; namely, the radial displacement gradually reduces with the increase in distance from the periphery. The difference is that the maximum displacement in this test (4 mm) is larger than that of the previous one (2.75 mm) [4] because the interface size of the parking lot in this study is larger than that of all the chambers in the previous test.

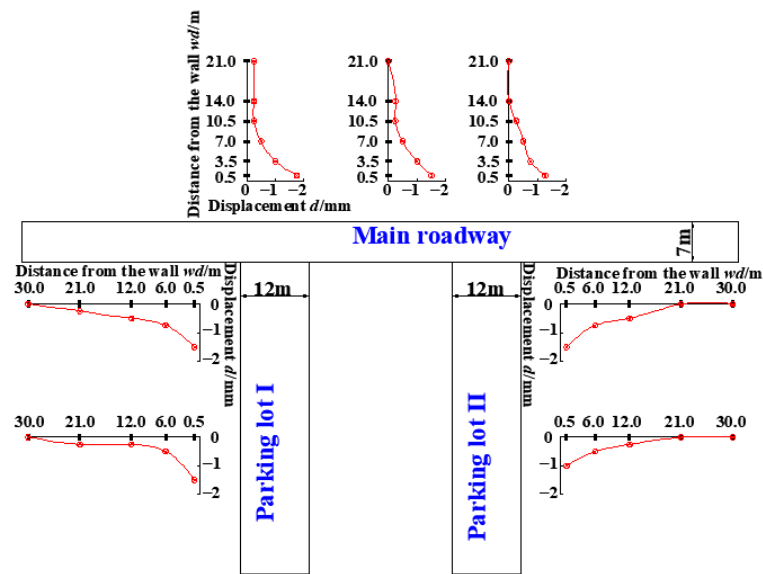


Figure 7. Variation of the radial displacement versus the distance from the periphery after the excavation of chambers.

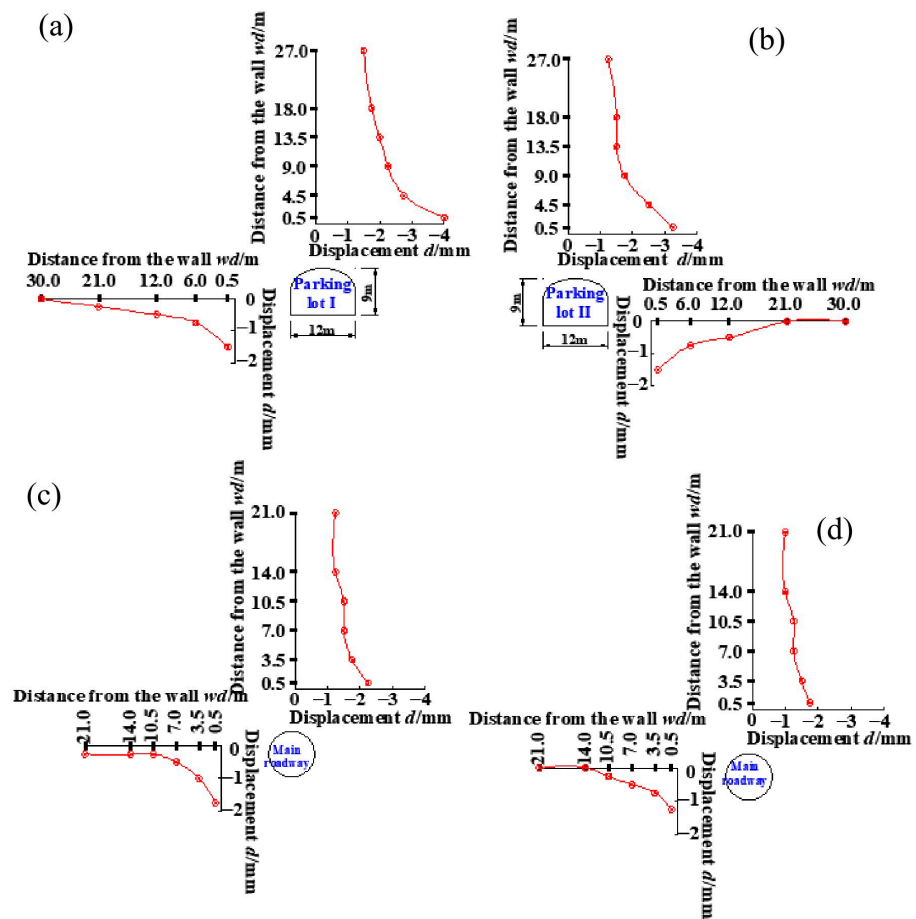


Figure 8. Variation of the radial displacement versus the distance from the periphery after the excavation of (a) parking lot I (in Section II); (b) parking lot II (in Section II); (c) the main roadway (in Section III); and (d) the main roadway (in Section IV).

After excavation, the displacement of the unsupported parking lot I is greater than that of the supported parking lot II at the same location. The displacement of the supported chamber is reduced by 14–22% compared with that of the unsupported chamber.

Figures 9 and 10 present the typical curves of radial stresses calculated from the strains measured by strain bricks after excavation. Figure 11 presents the typical stress curves measured by pressure cells after excavation. From these results, we concluded the following:

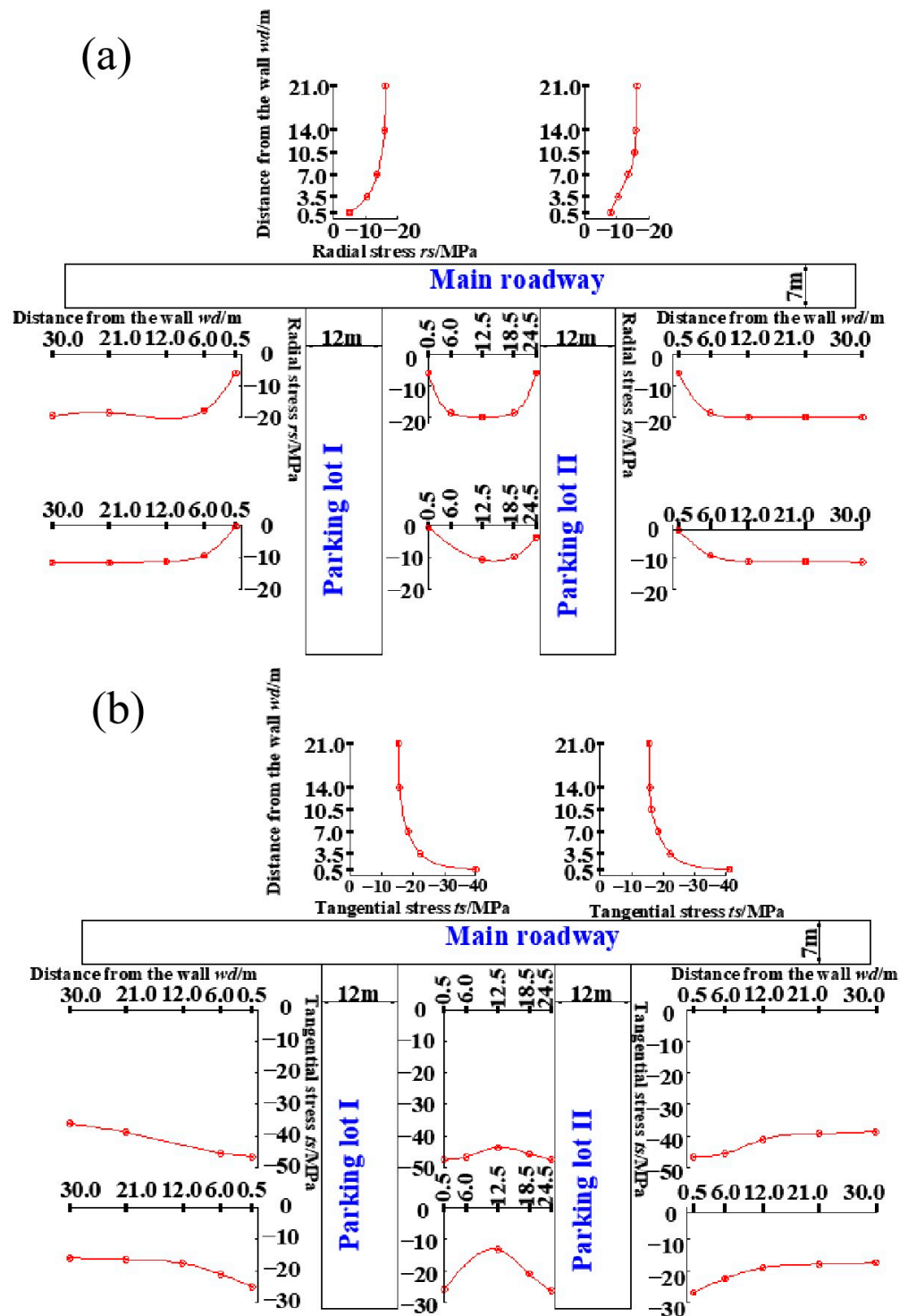


Figure 9. (a) Radial stress curves after the excavation by the strain bricks. (b) Tangential stress curves after the excavation measured by the strain bricks.

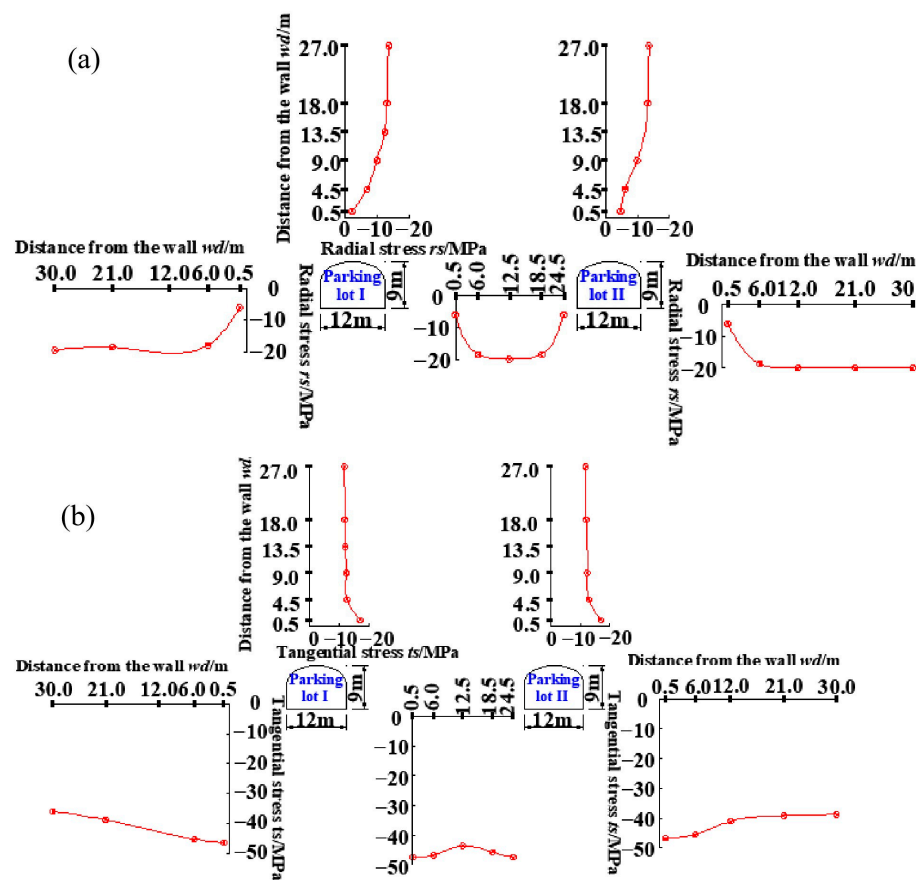


Figure 10. (a) Radial stress curves of the parking lots measured by the strain bricks (in Section II). (b) Tangential stress curves of the parking lots measured by the strain bricks (in Section II).

The variation of stress after excavation is basically the same as that of previous tests [31,45,53]; namely, the stress measured by the pressure cell and strain brick is basically the same. There is obvious interaction between the chambers during excavation, e.g., the stress curve of the middle part between two parking lots is parabolic rather than a monotonic decreasing trend. The difference is that the maximum tangential stress at the intersection in this experiment (46.67 MPa) is larger than that of the previous test (39.2 MPa) [31] because the interface size of the parking lot in this experiment is larger than that of all the chambers in the previous test.

3.5.2. Test Results of the Bolt

The axial force (N_i) of the bolt can be calculated by the following formula:

$$N_i = E_b \varepsilon_i \pi \varnothing^2 / 4 \quad (6)$$

where E_b , ε_i and \varnothing are the elastic modulus, monitored axial strain and bolt diameter, respectively.

Figure 12 shows the curve of the axial force along the bolt at Section M-1 after the chamber excavation. The experimental chamber is axisymmetrical, so the displacement of the symmetrical part of the supporting chamber can be compared with that of the unsupported chamber, to reveal the supporting effect of the bolt. As shown in Figure 5a, the selected parts of the red and blue border are two symmetrical parts, respectively. Comparison of the displacements between supported and unsupported chambers at the same position is shown in Figure 13.

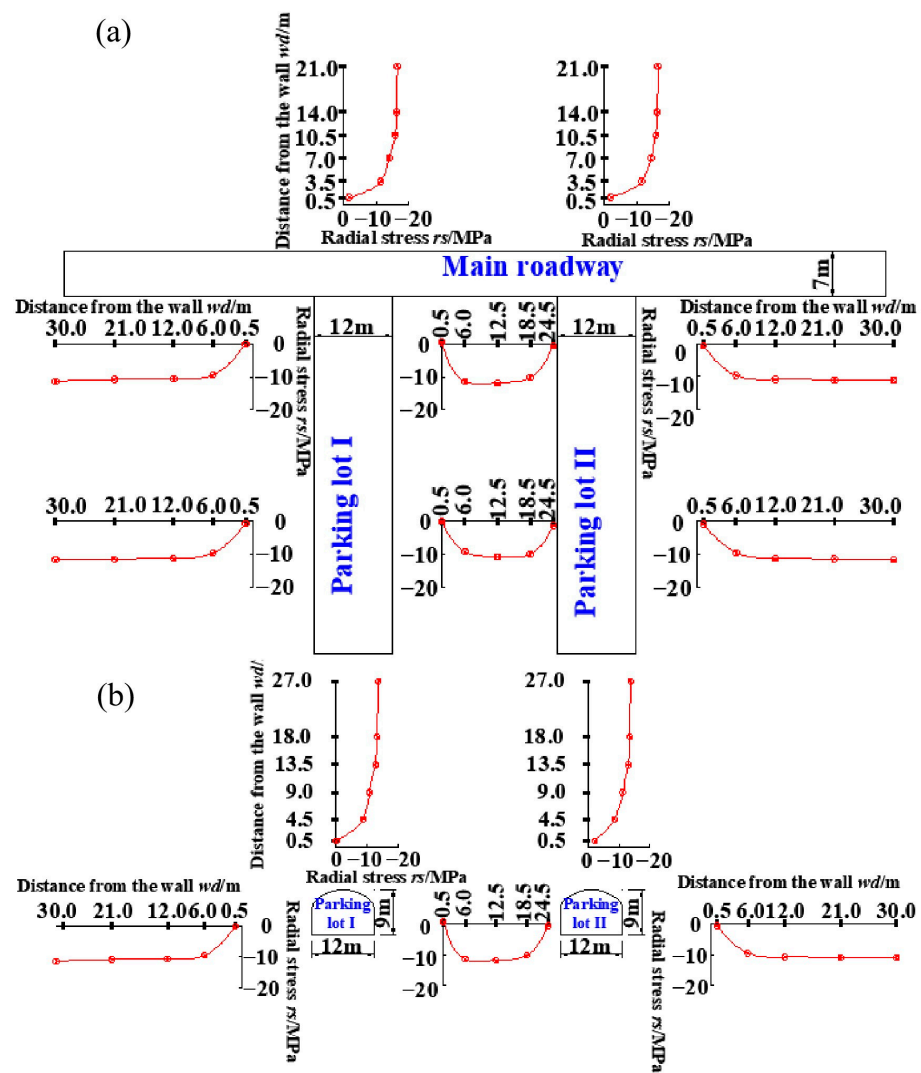


Figure 11. (a) The stress curves at the flat section after the excavation; (b) the stress curves of the parking lots after the excavation (in Section II).

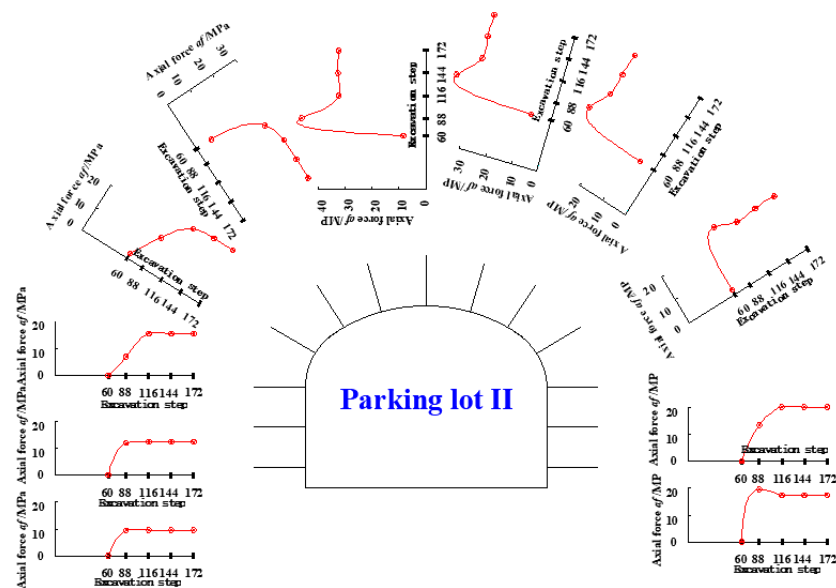


Figure 12. Curve of axial force of bolt with excavation step.

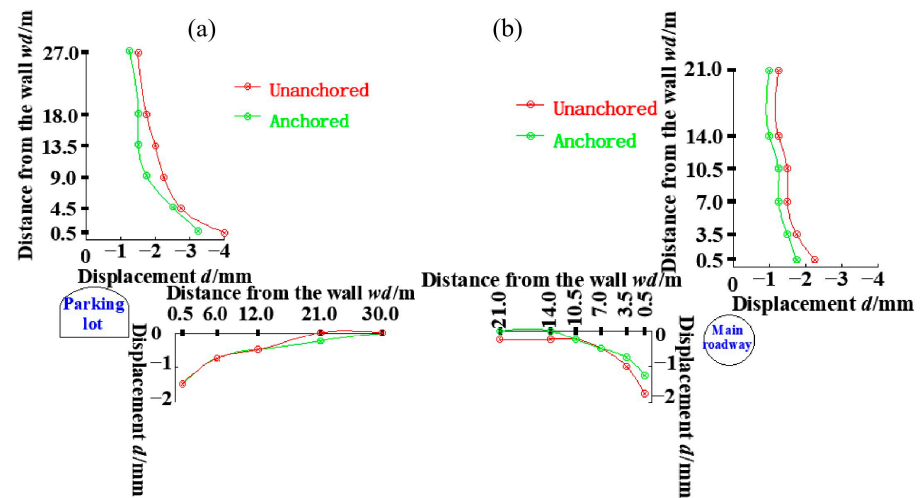


Figure 13. Contrast curve of displacement between supporting and unsupported measuring points in the same position around cavern: (a) Parking lot and (b) main roadway.

The following can be observed:

The axial force of the bolt is very small, which indicates the interaction between the bolt and rock is very weak before the chamber excavation. During the excavation of the upper and lower steps of the chamber where the embedded bolts are located, the axial force tends to increase rapidly. After the excavation, the axial force of the anchor tends to be stable.

After the excavation, the axial force of bolts is all tensile force. The tension of the bolt at the vault top is greater than that at the waist of the cave. This indicates that the supporting effect of the bolt at the vault top of the chamber is greater than that of the waist bolt.

The displacement of bolted measuring points in the same part of the chamber is less than that of non-bolted measuring points, and the deformation around the chamber decreases by about 14–22% after supporting, suggesting that bolt support controls the development of surrounding rock deformation.

The tensile force in the bolt around the chamber is not large, and the maximum is only 46.23 MPa, which is far lower than the ultimate strength of the bolt. All the bolts remain intact during the evolution process. These results demonstrate that the support scheme is reasonable and reliable.

4. Overloading Test

To further assess the overall safety factors of the URL, we carried out overloading tests on the model after the excavation.

The detailed steps of the overloading model test are as follows: (1) gradually increase crustal stress according to the growth rate of 0.1 times; (2) the stress at each stage is kept constant for half an hour and deformation and failure of the chamber group in real time are recorded; and (3) Steps (1) and (2) are repeated until the chamber group is completely destroyed. In order to observe and record the deformation and destruction of the chamber group in the process of overloading, four micro-HD cameras were placed at the specific locations shown in Figure 14a. Figure 14 shows the pictures of the model after excavation.

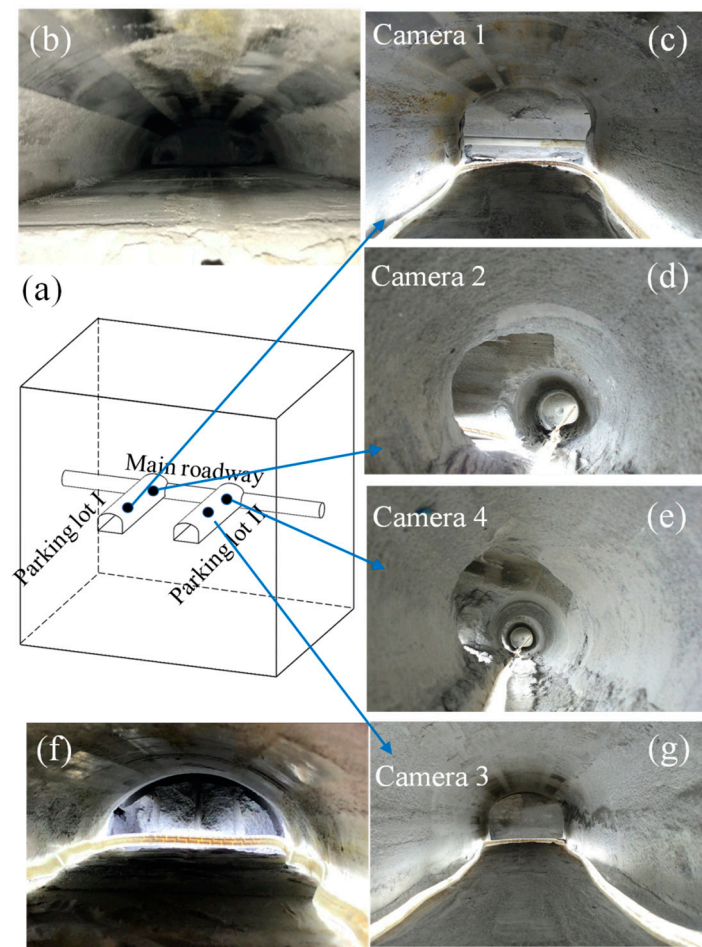


Figure 14. Pictures of the chamber group after excavation. (a) Layout diagram of micro cameras. (b) The picture of parking lot I after upper-bench excavation (taken by camera 1). (c) The picture of parking lot I after lower-bench excavation (taken by camera 1). (d) The picture of the main roadway after excavation (taken by camera 2). (e) The picture of the main roadway after excavation (taken by camera 4). (f) The picture of parking lot II after upper-bench excavation (taken by camera 3). (g) The picture of parking lot II after lower-bench excavation (taken by camera 3).

4.1. Process of the Overloading Test

The safety coefficient of overloading (K_S) is defined as the following formula:

$$K_s = \frac{P_f}{P_0} \quad (7)$$

where P_0 and P_f are the loads at the initial and failure stages, respectively.

K_S can especially be divided into three stages based on the displacement changes and the degree of failure of surrounding rock [45]:

$$K_{s1} = \frac{P_1}{P_0}; K_{s2} = \frac{P_2}{P_0}; K_{s3} = \frac{P_3}{P_0} \quad (8)$$

where K_{s1} , K_{s2} and K_{s3} are the safety coefficient of crack initiation, the safety coefficient of local destruction and the safety coefficient of general demolition, respectively. P_1 , P_2 and P_3 are the loads when the crack initiation, local destruction and general demolition start to appear, respectively.

4.2. Destruction Phenomena and Fracturing Patterns

The evolution of fractures at different intersection areas during the overloading test is shown in Figures 15–18. We can observe the following from these pictures:

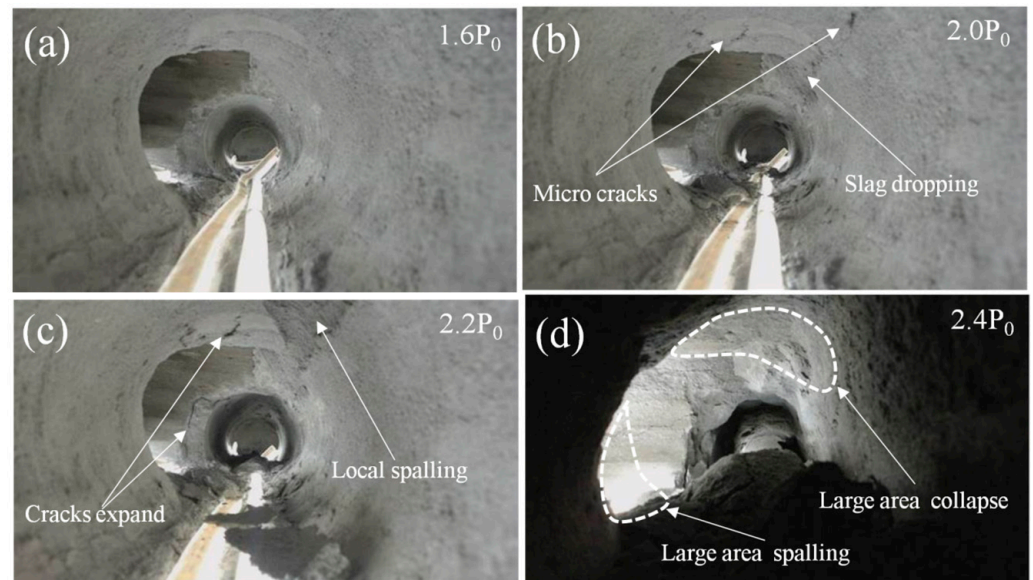


Figure 15. Fracture situation at the intersection area of the main roadway and parking lot I in the overloading stage of (a) $1.6 P_0$; (b) $2.0 P_0$; (c) $2.2 P_0$; and (d) $2.4 P_0$, respectively (taken by camera 2).

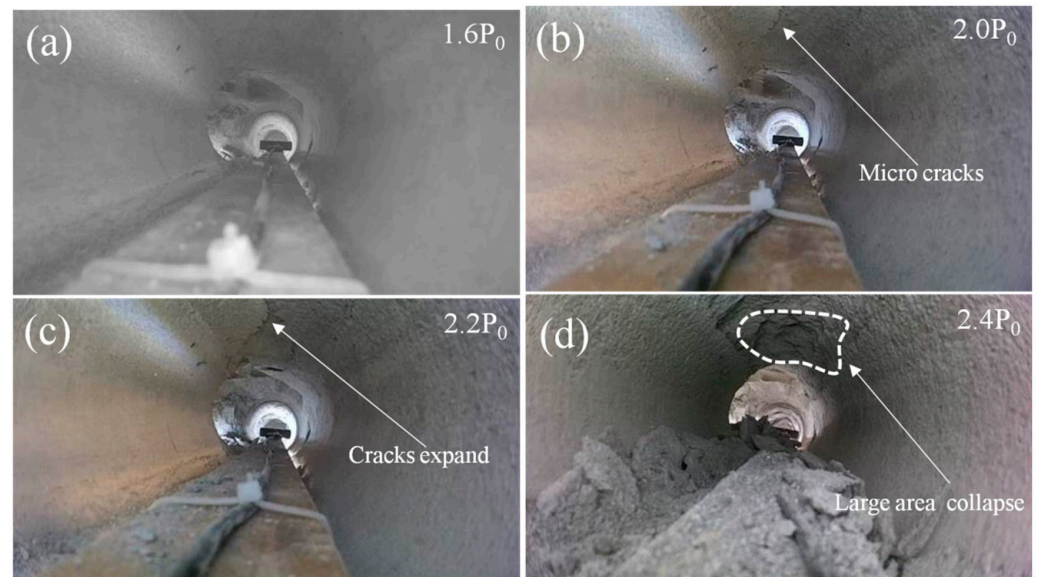


Figure 16. Fracture situation at the intersection area of the main roadway and parking lot II in the overloading stage of (a) $1.6 P_0$; (b) $2.0 P_0$; (c) $2.2 P_0$; and (d) $2.4 P_0$, respectively (taken by camera 4).

In the overloading stage of 1.1 – $1.6 P_0$, the interior of each chamber and the intersection parts are intact without any obvious cracks in the surrounding rock (see Figures 15a, 16a, 17a and 18a). Therefore, the URL is in a stable state under overloading of 1.1 – $1.6 P_0$.

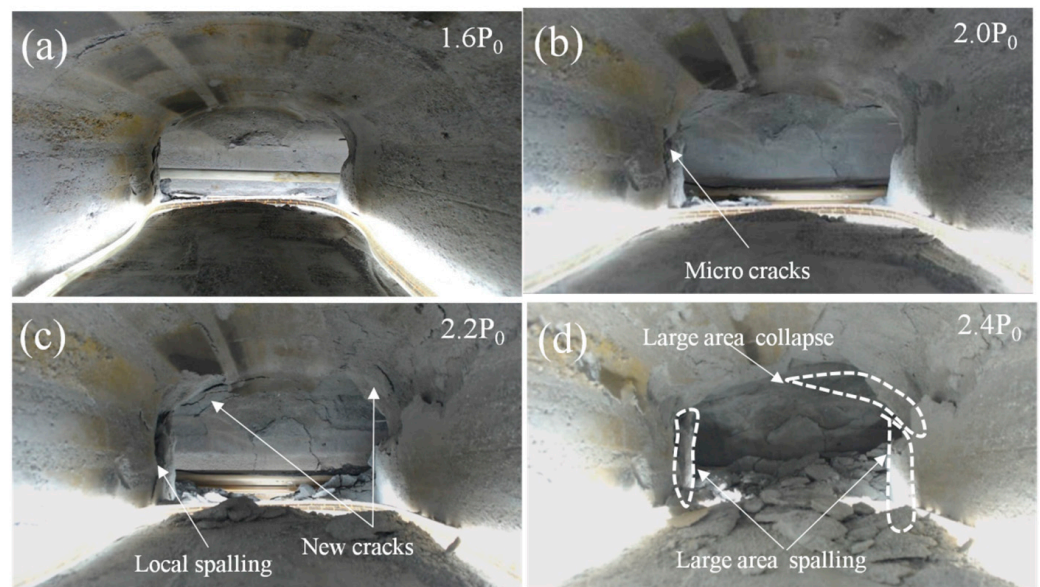


Figure 17. Fracture situation at parking lot I in the overloading stage of (a) $1.6 P_0$; (b) $2.0 P_0$; (c) $2.2 P_0$; and (d) $2.4 P_0$, respectively (taken by camera 1).

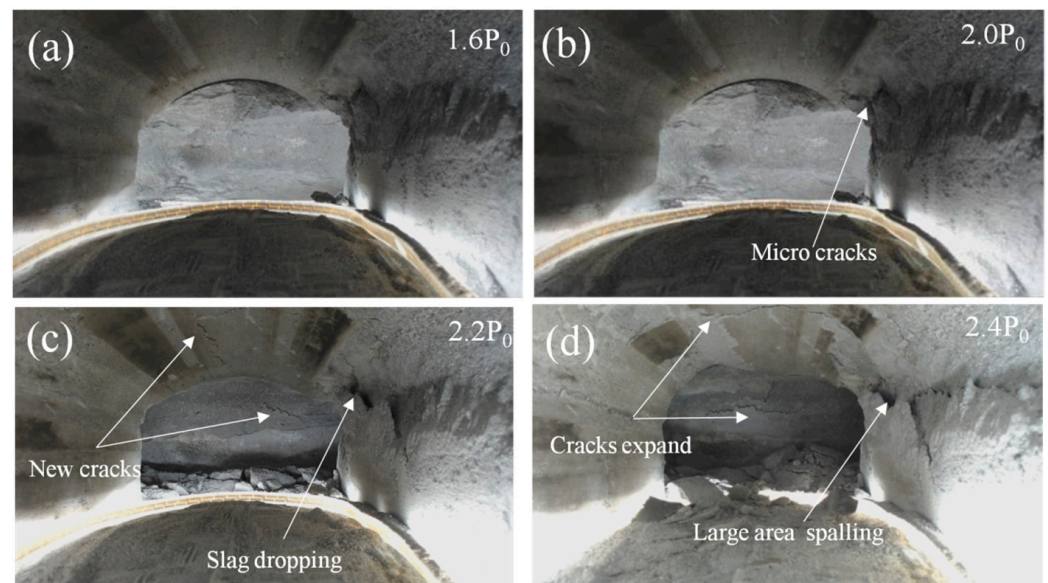


Figure 18. Fracture situation at parking lot II in the overloading stage of (a) $1.6 P_0$; (b) $2.0 P_0$; (c) $2.2 P_0$; and (d) $2.4 P_0$, respectively (taken by camera 1).

When the loading exceeds $1.6 P_0$, some visible micro cracks appear at the intersection area of the chambers. When overloading increases to $2.0 P_0$, slag dropping phenomena appear locally, mainly concentrating at the following locations:

(1) Micro cracks and slag dropping appear at the intersecting roof of the main roadway and parking lot I (hereinafter, RP1) (Figure 15b). (2) Horizontal micro cracks appear at the intersecting roof of the main roadway and parking lot II (hereinafter, RP2) (Figure 16b). (3) Vertical micro cracks appear at the intersecting waist of parking lot I and the main roadway (hereinafter, WP1) (Figure 17b). (4) Micro cracks appear at the intersecting corner of parking lot II and the main roadway (hereinafter, CP2) (Figure 18b).

In the overloading stage of $2.1\sim 2.2 P_0$, the micro cracks in the chamber began to expand gradually. With the continuous increase in overloading, the cracks in the chamber gradually changed from narrow to wide, and from short to long, which led local compression–shear

and tensile–shear failures to appear in the surrounding rock, specifically manifesting as: (1) Local spalling failures constantly appear at RP1 (see Figure 15c); the initial micro cracks at these interaction areas gradually expand, accompanied by a new vertical fracture emerging at WP1 (Figure 15c). (2) The initial horizontal micro crack at RP2 gradually expands and leads to a horizontal fracture, which is about 1 mm wide (Figure 16c). (3) The initial vertical micro cracks at WP1 gradually expand and lead to local spalling. Several cracks emerge at RP1 (site XX in Figure 17c). (4) Slag dropping appears at the CP2 (Figure 18c).

In the overloading stage of $2.4 P_0$, obvious deformation and failure phenomena appear in each part of the chamber groups. This specifically manifests in the following: (1) A large area of collapse appears at RP1. Obvious shrinkage deformation occurs on both sides of the main roadway (Figure 15d). (2) A large area of collapse appears at RP1 (Figure 16d). (3) The cracks at the intersection of parking lot I and the main roadway expand along the wall rapidly. After the formation of the penetrating cracks, the large area of collapse and spalling failures occur (Figure 17d). (4) Parking lot II produces long transverse cracks along the axis of the chamber, causing side walls to be damaged with a large area of spalling (Figure 18d).

4.3. Overloading Induced Deformation

Figure 19 shows the spatial variation of the radial displacements in the horizontal cross-section during overloading while Figure 20 shows the displacements in the vertical cross-section. Figure 21 shows the displacement change curves of Section I in the overloading stage.

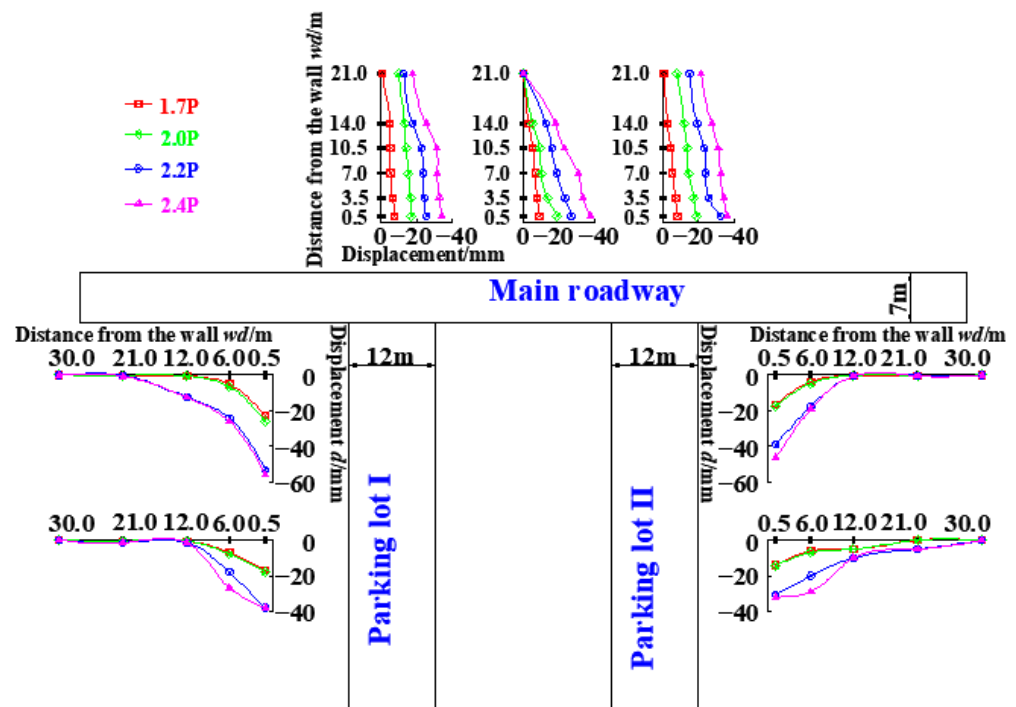


Figure 19. The spatial variation of the radial displacements in the horizontal cross-section in the overloading stage.

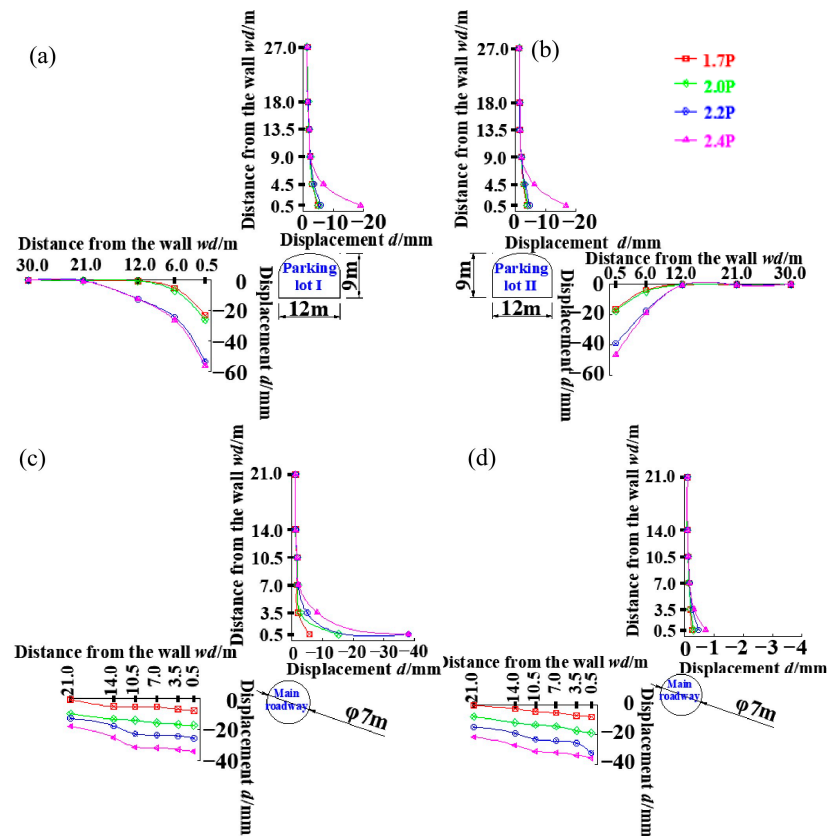


Figure 20. The spatial variation in the radial displacements in the stage of overloading on the horizontal cross-section: (a) parking lot I (in Section II); (b) parking lot II (in Section II); (c) main roadway (in Section III); and (d) main roadway (in Section IV).

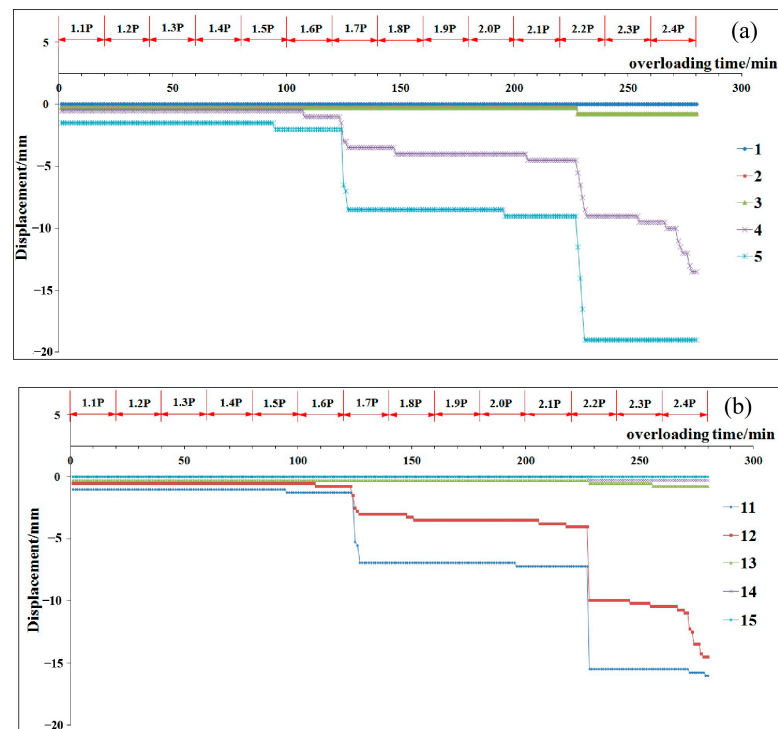


Figure 21. The time history of displacements of the parking lots in Section II during the overloading test. (a) Parking lot I and (b) parking lot II.

From these figures, we concluded the following:

With ongoing overloading, the deformation around the chamber increases gradually. The deformation of the unsupported parking lot (parking lot I) is obviously larger than that of the supported one (parking lot II). The deformation of the unsupported parking lot is about 0–25% less than that of the supported one.

When overloading is stable, the displacement of each chamber increases in varying degrees, and then tends to be stable. With the increase in multiple overloading, the slope of the displacement curve of each chamber increases gradually. During the whole overloading process, the maximum displacement is –160.00 mm, which appears in RP1.

We can maintain that without the support, the safety coefficient of crack initiation is 1.7, the safety coefficient of local destruction is 2.1 and the safety coefficient of general demolition is 2.3. Corresponding with the support, the safety coefficient of crack initiation is 1.9, the safety coefficient of local destruction is 2.2 and the safety coefficient of general demolition is 2.4.

4.4. Discussions

The safety factor after support has been improved, and all the safety factors in this study are smaller than those obtained in previous studies [31,45]. It shows that the interface size of the chamber has obvious influence on the safety factor.

The study of overload tests found that the failure of surrounding rock firstly occurs in the intersection area of the chamber group, and the damage degree in the intersection area is significantly more severe than in other parts. This is also consistent with previous studies [31,45].

5. Conclusions

Three-dimensional physical model tests were carried out on a deep underground chamber group consisting of a main roadway and two parking lots (one was supported, the other was not supported), and the engineering background was the URL of HLW for the geological disposal in Beishan. We have reached the following conclusions:

- (1) After the excavation, convergent deformation occurs in the surrounding rock with the maximum value of more than 4 mm. The displacement of the intersection is 7–33% larger than that of the non-intersection. The displacement of the supporting chamber is reduced by 14–22% compared with that of the unsupported chamber.
- (2) After the excavation, the axial force of bolts is all tensile force. The tension of the bolt at the vault top is greater than that at the waist of the cave, indicating that the supporting effect of the bolt at the vault top of the chamber is greater than that of the waist bolt.
- (3) Support significantly increased the safety factor. Specifically, the safety coefficient of crack initiation is increased from 1.7 to 1.9, the safety coefficient of local destruction is increased from 2.1 to 2.2 and the safety coefficient of general demolition is increased from 2.3 to 2.4.
- (4) The failure of surrounding rock firstly occurs in the intersection area of the chamber group, and the damage degree in the intersection area is significantly more severe than in other parts. Therefore, intensive monitoring should be performed on the large intersection, and appropriate support should be carried out according to the monitoring results. In the next step, we will improve the traditional strength reduction method based on the safety factor obtained from the research to obtain a more accurate and reliable numerical calculation method for evaluating the safety factor of the chamber group.

Author Contributions: C.L. contributed to the Data curation, Writing of this article and Investigation. X.S. and X.Z. contributed to the Supervision. Q.Z. contributed to the Writing—review and editing of this article. Y.C. and J.W. contributed to the Data curation and Investigation. All authors have read and agreed to the published version of the manuscript.

Funding: This research was funded by the Shandong Province Postdoctoral Innovation Project (SDCX-ZG-202203055), the preliminary research project of the underground laboratory for the geological disposal of high-level radioactive waste of China (No. YK-KY-J-2015-25), the National Key Research and Development Project (2020YFB1314200) and the Major Scientific and Technological Innovation Project in Shandong Province (No. 2019SDZY02).

Institutional Review Board Statement: Not applicable.

Informed Consent Statement: Not applicable.

Data Availability Statement: Corresponding authors can provide more details regarding where data supporting reported results through email.

Acknowledgments: We want to deliver our sincere gratitude to those who made arduous efforts in reviewing this article and to the editors.

Conflicts of Interest: The authors declare that they have no conflict of interest.

References

1. Wang, J.; Pang, Z. *Chapter 17 Comparison Between Geological Disposal of Carbon Dioxide and Radioactive Waste in China*; Springer Science and Business Media LLC: Berlin, Germany, 2011.
2. Wang, J.; Chen, L.; Su, R.; Zhao, X.G. The Beishan underground research laboratory for geological disposal of high-level radioactive waste in China: Planning, site selection, site characterization and in situ tests. *J. Rock Mech. Geotech. Eng.* **2018**, *10*, 411–435. [[CrossRef](#)]
3. Li, J.; Su, R.; Zhou, Z. The Single Deposit Scale Scenario at Granite Area in A Long-Term Safety Assessment of A Radioactive Waste Repository. *IOP Conf. Ser. Earth Environ. Sci.* **2019**, *237*, 022012. [[CrossRef](#)]
4. Hou, J.X.; Wu, Y.D.; Xu, Y.J.; Li, X.J.; Wang, S.; Wang, F.P.; Zhang, X.R. 3D Data Visualization System of Immersive Underground Laboratory. *Sustain. Cities Soc.* **2019**, *46*, 101439. [[CrossRef](#)]
5. Zhang, C.L.; Wang, J.; Su, K. Concepts and tests for disposal of radioactive waste in deep geological formations. *Chin. J. Rock Mech. Eng.* **2006**, *25*, 750–767.
6. NEA (Nuclear Energy Agency). *The Role of Underground Laboratories in Nuclear Waste Disposal Programmes*; OECD Publications: Paris, France, 2001.
7. Wang, J.; Chen, W.M.; Su, R. Geological disposal of high-level radioactive waste and its key scientific issues. *Chin. J. Rock Mech. Eng.* **2006**, *4*, 801–812.
8. Wang, J. On area-specific underground research laboratory for geological disposal of high-level radioactive waste in China. *J. Rock Mech. Geotech. Eng.* **2014**, *6*, 99–104. [[CrossRef](#)]
9. Delay, J.; Lebon, P.; Rebours, H. Meuse/Haute-Marne centre: Next steps towards a deep disposal facility. *J. Rock Mech. Geotech. Eng.* **2010**, *2*, 52–70.
10. Comino, J.Á.L.; Heimann, S.; Cesca, S.; Claus, M.; Dahm, T.; Zang, A. Automated Full Waveform Detection and Location Algorithm of Acoustic Emissions from Hydraulic Fracturing Experiment. *Procedia Eng.* **2017**, *191*, 697–702. [[CrossRef](#)]
11. Liu, J.F.; Chen, L.; Wang, C.P.; Man, K.; Wang, L.; Wang, J.; Su, R. Characterizing the mechanical tensile behavior of Beishan granite with different experimental methods. *Int. J. Rock Mech. Min. Sci.* **2014**, *69*, 50–58. [[CrossRef](#)]
12. Man, K.; Liu, X.L.; Gong, F.Q.; Ma, H.S.; Chen, Z.M.; Wang, J. Static & dynamic properties of granite in Xinjiang's Tianhu area as a pre-selected geological disposal site of HLW. *Vib. Shock.* **2007**, *36*, 146–156.
13. Vasconcelos, R.G.W.; Beaudoin, N.; Hamilton, A.; Hyatt, N.C.; Provis, J.L.; Corkhill, C.L. Characterisation of a high pH cement backfill for the geological disposal of nuclear waste: The Nirex Reference Vault Backfill. *Appl. Geochem.* **2018**, *89*, 180–189. [[CrossRef](#)]
14. Pushkareva, R.; Kalinichenko, E.; Lytovchenko, A.; Pushkarev, A.; Kadochnikov, V.; Plastynina, M. Irradiation effect on physico-chemical properties of clay minerals. *Appl. Clay Sci.* **2002**, *21*, 117–123. [[CrossRef](#)]
15. Tripathi, K.K.; Viswanadham, B.V.S. Evaluation of the Permeability Behaviour of Sand-Bentonite Mixtures Through Laboratory Tests. *Indian Geotech. J.* **2012**, *42*, 267–277. [[CrossRef](#)]
16. Akügn, H.; Ada, M.; Koçkar, M.K. Performance assessment of a bentonite–sand mixture for nuclear waste isolation at the potential Akkuyu Nuclear Waste Disposal Site, southern Turkey. *Environ. Earth Sci.* **2015**, *73*, 6101–6116. [[CrossRef](#)]
17. Mokni, N.; Barnichon, J.D. Hydro-mechanical analysis of SEALEX in-situ tests-Impact of technological gaps on long term performance of repository seals. *Eng. Geol.* **2016**, *205*, 81–92. [[CrossRef](#)]
18. Hajj, H.E.; Abdelouas, A.; Mendili, Y.E.; Karakurt, G.; Grambow, B.; Martin, C. Corrosion of carbon steel under sequential aerobic–anaerobic environmental conditions. *Corros. Sci.* **2013**, *76*, 432–440. [[CrossRef](#)]
19. King, F. Predicting the Lifetimes of Nuclear Waste Containers. *J. Miner. Met. Mater. Soc.* **2014**, *66*, 526–537. [[CrossRef](#)]
20. Ahn, T.M. Multiple lines of evidence for performance of the canister and waste form in long-term nuclear waste disposal: Reviews. *Prog. Nucl. Energy* **2016**, *93*, 343–350. [[CrossRef](#)]

21. Andersson, P.; Byegård, J.; Tullborg, E.L.; Doe, T.; Hermanson, J.; Winberg, A. In situ tracer tests to determine retention properties of a block scale fracture network in granitic rock at the Äspö Hard Rock Laboratory, Sweden. *J. Contam. Hydrol.* **2004**, *70*, 271–297. [[CrossRef](#)] [[PubMed](#)]
22. Walton, G.; Lato, M.; Anshütz, H.; Perras, M.A.; Diederichs, M.S. Non-invasive detection of fractures, fracture zones, and rock damage in a hard rock excavation-Experience from the Äspö Hard Rock Laboratory in Sweden. *Eng. Geol.* **2015**, *196*, 210–221. [[CrossRef](#)]
23. Zhang, Z.X.; Kou, S.Q.; Lindqvist, P.A. In-situ measurements of TBM cutter temperature in Äspö Hard Rock Laboratory, Sweden. *Int. J. Rock Mech. Min. Sci.* **2001**, *38*, 585–590. [[CrossRef](#)]
24. Liu, Y.M.; Wang, J.; Cao, S.F.; Ma, L.K.; Xie, J.L.; Zhao, X.G.; Chen, L. A large-scale THMC experiment of buffer material for geological disposal of high level radioactive waste in China. *Rock Soil Mech.* **2013**, *34*, 2756–2762+2789.
25. Chen, L.; Liu, Y.M.; Wang, J.; Cao, S.F.; Xie, J.L.; Ma, L.K.; Zhao, X.G.; Li, Y.W.; Liu, J. Investigation of the thermal-hydro-mechanical (THM) behavior of GMZ bentonite in the China-Mock-up test. *Eng. Geol.* **2014**, *172*, 57–68. [[CrossRef](#)]
26. Cho, W.J.; Kim, J.S.; Lee, C.S.; Kwon, S.; Choi, J.W. In situ experiments on the performance of near-field for nuclear waste repository at KURT. *Nucl. Eng. Des.* **2014**, *252*, 278–288. [[CrossRef](#)]
27. Snow, M.S.; Clark, S.B.; Morrison, S.S.; Watrous, M.G.; Olson, J.E.; Snyder, D.C. Mechanical environmental transport of actinides and 137Cs from an arid radioactive waste disposal site. *J. Environ. Radioact.* **2015**, *148*, 45–48. [[CrossRef](#)] [[PubMed](#)]
28. Armand, G.; Bumbieler, F.; Conil, N.; Vaissière, R.; Bosgiraud, J.M.; Vu, M.N. Main outcomes from in situ thermo-hydro-mechanical experiments programme to demonstrate feasibility of radioactive high-level waste disposal in the Callovo-Oxfordian claystone. *J. Rock Mech. Geotech. Eng.* **2017**, *9*, 415–427. [[CrossRef](#)]
29. Denise-Penelope, K.; Ahmed, F. 3D FEM Analysis of a Pile-Supported Riverine Platform under Environmental Loads Incorporating Soil-Pile Interaction. *Computation* **2018**, *6*, 10.
30. Zhang, Q.Y.; Ren, M.Y.; Duan, K.; Wang, W.S.; Gao, Q.; Lin, H.X.; Xiang, W.; Jiao, Y.Y. Geo-mechanical model test on the collaborative bearing effect of rock-support system for deep tunnel in complicated rock strata. *Tunn. Undergr. Space Technol.* **2019**, *91*, 103001. [[CrossRef](#)]
31. Zhang, Q.; Liu, C.; Duan, K.; Zhang, Z.; Xiang, W. True Three-Dimensional Geomechanical Model Tests for Stability Analysis of Surrounding Rock During the Excavation of a Deep Underground Laboratory. *Rock Mech. Rock Eng.* **2020**, *53*, 517–537. [[CrossRef](#)]
32. He, C.C.; Hu, X.L.; Dwayne, D.; Tan, F.L.; Zhang, Y.M.; Zhang, H. Response of a landslide to reservoir impoundment in model tests. *Eng. Geol.* **2018**, *247*, 84–93. [[CrossRef](#)]
33. Zhang, S.; Zhang, X.C.; Pei, X.J.; Wang, S.Y.; Huang, R.H.; Xu, Q.; Wang, Z.L. Model test study on the hydrological mechanisms and early warning thresholds for loess fill slope failure induced by rainfall. *Eng. Geol.* **2019**, *258*, 105–135. [[CrossRef](#)]
34. Shin, J.H.; Choi, Y.K.; Kwon, O.Y.; Lee, S.D. Model testing for pipe-reinforced tunnel heading in a granular soil. *Tunn. Undergr. Space Technol.* **2008**, *23*, 241–250. [[CrossRef](#)]
35. Hu, X.D.; Fang, T.; Chen, J.; Hui, R.; Wang, G. A large-scale physical model test on frozen status in freeze-sealing pipe roof method for tunnel construction. *Tunn. Undergr. Space Technol.* **2018**, *72*, 55–63. [[CrossRef](#)]
36. Bao, Z.; Yuan, Y.; Yu, H.T. Multi-scale physical model of shield tunnels applied in shaking table test. *Soil Dyn. Earthq. Eng.* **2017**, *100*, 465–479. [[CrossRef](#)]
37. Zhu, W.S.; Zhang, Q.B.; Li, Y.; Sun, L.F.; Zhang, L.; Zheng, W.H. Development of large-scale physical model test system under true triaxial loading and its applications. *Chin. J. Rock Mech. Eng.* **2010**, *29*, 1–7.
38. Li, Z.K.; Liu, H.; Dai, R.; Su, X. Application of numerical analysis principles and key technology for high fidelity simulation to 3-D physical model tests for underground caverns. *Tunn. Undergr. Space Technol.* **2005**, *20*, 390–399. [[CrossRef](#)]
39. Lin, P.; Liu, H.Y.; Zhou, W.Y. Experimental study on failure behaviour of deep tunnels under high in-situ stresses. *Tunn. Undergr. Space Technol.* **2015**, *46*, 28–45. [[CrossRef](#)]
40. Wang, S.G.; Liu, Y.R.; Tao, Z.F.; Zhang, Y.; Zhong, D.N.; Wu, Z.S.; Lin, C.; Yang, Q. Physical model test for failure and stability analysis of high arch dam based on acoustic emission technique. *Int. J. Rock Mech. Min. Sci.* **2018**, *112*, 95–107. [[CrossRef](#)]
41. Chen, H.M.; Yu, H.S.; Smith, M.J. Physical model tests and numerical simulation for assessing the stability of brick-lined tunnels. *Tunn. Undergr. Space Technol.* **2016**, *53*, 109–119. [[CrossRef](#)]
42. Zhang, Q.B.; He, L.; Zhu, W.S. Displacement measurement techniques and numerical verification in 3D physical model tests of an underground cavern group. *Tunn. Undergr. Space Technol.* **2016**, *56*, 54–56. [[CrossRef](#)]
43. Zhu, W.S.; Li, Y.; Li, S.C.; Wang, S.G.; Zhang, Q.B. Quasi-three-dimensional physical model tests on a cavern complex under high in-situ stresses. *Int. J. Rock Mech. Min. Sci.* **2011**, *48*, 199–209.
44. Nunes, M.A.; Meguid, M.A. A study on the effects of overlying soil strata on the stresses developing in a tunnel lining. *Tunn. Undergr. Space Technol.* **2009**, *24*, 716–722. [[CrossRef](#)]
45. Zhang, Q.Y.; Zhang, Y.; Duan, K.; Liu, C.C.; Miao, Y.S.; Wu, D. Large-scale geo-mechanical model tests for the stability assessment of deep underground complex under true-triaxial stress. *Tunn. Undergr. Space Technol.* **2019**, *83*, 577–591. [[CrossRef](#)]
46. Zhao, X.G.; Wang, J.; Cai, M.; Ma, L.K.; Zong, Z.H.; Wang, X.Y.; Su, R.; Chen, W.M.; Zhao, H.G.; Chen, Q.C.; et al. In-situ stress measurements and regional stress field assessment of the Beishan area. *Eng. Geol.* **2013**, *163*, 26–40. [[CrossRef](#)]
47. Fumagalli, I.E. *Static and Geomechanical Models*; Springer: New York, NY, USA, 1973.
48. Zhang, Q.Y.; Duan, K.; Jiao, Y.Y.; Xiang, W. Physical model test and numerical simulation for the stability analysis of deep gas storage cavern group located in bedded rock salt formation. *Int. J. Rock Mech. Min. Sci.* **2017**, *94*, 43–54. [[CrossRef](#)]

49. Zhang, Q.Y.; Zhang, X.T.; Wang, Z.C.; Xiang, W.; Xue, J.H. Failure mechanism and numerical simulation of zonal disintegration around a deep tunnel under high stress. *Int. J. Rock Mech. Min. Sci.* **2017**, *93*, 344–355. [[CrossRef](#)]
50. Chen, X.G.; Zhang, Q.Y.; Wang, Y.; Liu, D.J.; Zhang, N. Model test of anchoring effect on zonal disintegration in deep surrounding rock masses. *Sci. World J.* **2013**, *2013*, 935148. [[CrossRef](#)]
51. Zhang, Q.Y.; Li, S.C.; Zhu, W.S.; You, C.A.; Guo, X.H.; Ma, G.L.; Chen, J.G.; Li, Y.; Wang, H.P. Cementitious Geotechnical Analogue Material for Iron Crystal Sand and Preparation Method. China Patent CN1792990, 28 June 2006.
52. Li, S.C.; Liu, Q.; Li, L.P.; Zhao, Y.; Wang, H.P.; Zhao, Y.; Yuan, X.S. Development of large-scale geomechanical model test system for tunnel construction and its application. *Chin. J. Rock Mech. Eng.* **2011**, *30*, 1368–1374.
53. Liu, C.; Zhang, Q.; Duan, K.; Xiang, W.; Jiao, Y. Development and Application of an Intelligent Test System for the Model Test on Deep Underground Rock Caverns. *Energies* **2020**, *13*, 358. [[CrossRef](#)]

Disclaimer/Publisher’s Note: The statements, opinions and data contained in all publications are solely those of the individual author(s) and contributor(s) and not of MDPI and/or the editor(s). MDPI and/or the editor(s) disclaim responsibility for any injury to people or property resulting from any ideas, methods, instructions or products referred to in the content.